

# Investigations of fast processes by X-ray diffraction methods at the Siberian Synchrotron and Terahertz Radiation Center

V M Aulchenko, V V Zhulanov, G N Kulipanov, K A Ten, B P Tolochko, L I Shekhtman

DOI: <https://doi.org/10.3367/UFNe.2018.01.038339>

## Contents

<b>1. Introduction</b>	<b>515</b>
1.1 Historical reference; 1.2 Onset and progress of work to use synchrotron radiation in Novosibirsk	
<b>2. Development of fast one-coordinate X-ray detectors at the BINP Physics</b>	<b>517</b>
<b>3. Experimental stations of time-resolved diffractometry at the Siberian Synchrotron and Terahertz Radiation Center</b>	<b>517</b>
3.1 Time-resolved experimental station ‘Diffraction movie’ in channel 5-b of the VEPP-3 storage ring; 3.2 ‘Explosion’ station in channel 0-b of VEPP-3; 3.3 ‘Precision diffractometry’ station in channel 6 of VEPP-3; 3.4 ‘Hard X-ray diffractometry’ station in channel 4 of VEPP-3	
<b>4. Time-resolved diffraction experiments at the Siberian Synchrotron and Terahertz Radiation Center</b>	<b>520</b>
4.1 Self-propagating high-temperature synthesis; 4.2 Detonation and shock-wave action; 4.3 Detonation nanodiamond synthesis from high explosives with a negative oxygen balance; 4.4 Behavior of nanodiamonds artificially introduced into a detonation wave; 4.5 Variation of hydrodynamic expansion conditions of detonation products as a tool to control the kinetics of nanodiamond growth; 4.6 Shock-wave synthesis of Ag, Bi, Co, and Pb nanoparticles; 4.7 Phase transitions in the course of preparation and activation of Co–Al catalysts for Fischer–Tropsch synthesis; 4.8 Phase composition and structural transformations in strontium cobaltite ceramics under heating in different conditions; 4.9 Interaction of gaseous hydrogen with metals; 4.10 Lithium intercalation–deintercalation mechanism in nanodimensional cathode materials for lithium-ion batteries; 4.11 Processes at the electrolyte–solid electrode interface; 4.12 Synthesis of nickel tungstate; 4.13 Synthesis of nickel molybdate; 4.14 Three-dimensional colloidal crystal formation; 4.15 Interaction dynamics of solid metals with liquid ones	
<b>5. Conclusions</b>	<b>530</b>
<b>References</b>	<b>530</b>

**Abstract.** A unique instrumentation complex that includes wigglers, X-ray position sensitive detectors, diffractometers, and explosion chambers and enables a 73 ps X-ray diffraction time resolution (exposure time) has been developed at the Siberian Synchrotron and Terahertz Radiation Center, a research colla-

boration operating at the Budker Institute of Nuclear Physics, Siberian Branch of the Russian Academy of Sciences. A number of techniques have been developed and implemented with which nanosecond-resolution investigations of the nucleation and growth dynamics became possible for the first time for diamond and metal nanoparticles under explosion and shock wave conditions. Studies with millisecond resolution of the structural transformation dynamics of chemical reactions, investigations of the kinetics of self-propagating high-temperature synthesis, and obtaining information on the state of catalysts are also among the new possibilities developed.

**Keywords:** synchrotron radiation, X-ray detectors, time resolution, nanosecond, detonation, shock wave, nanocolloidal crystal, solid state chemical reaction, self-propagating high-temperature synthesis — SHS, nanoparticle, phase transition, liquid metal, catalysis, hydrates

## 1. Introduction

Recent years have seen considerable progress in time-resolved X-ray diffractometry. This is due to the development of acceleration technology, the techniques of synchrotron radiation (SR) generation, and fast one- and two-coordinate fast X-ray detectors. A significant contribution to the development of time-resolved X-ray diffractometry with SR radiation beams was made by the scientists of the Siberian

V M Aulchenko, V V Zhulanov, G N Kulipanov, L I Shekhtman  
Budker Institute of Nuclear Physics, Siberian Branch of the Russian Academy of Sciences,  
prosp. Akademika Lavrent'eva 11, 630090 Novosibirsk, Russian Federation  
K A Ten Lavrent'ev Institute of Hydrodynamics, Siberian Branch of the Russian Academy of Sciences,  
prosp. Akademika Lavrent'eva 15, 630090 Novosibirsk, Russian Federation  
B P Tolochko Budker Institute of Nuclear Physics, Siberian Branch of the Russian Academy of Sciences,  
prosp. Akademika Lavrent'eva 11, 630090 Novosibirsk, Russian Federation;  
Institute of Solid State Chemistry and Mechanochemistry, Siberian Branch of the Russian Academy of Sciences,  
ul. Kutateladze 18, 630128 Novosibirsk, Russian Federation  
E-mail: B.P.Tolochko@inp.nsk.su

Received 15 January 2018, revised 19 January 2018  
*Uspekhi Fizicheskikh Nauk* **188** (6) 577–594 (2018)  
DOI: <https://doi.org/10.3367/UFNr.2018.01.038339>  
Translated by E N Ragozin; edited by A M Semikhatov

Branch of the Russian Academy of Sciences. This review describes the main operational facilities that use time-resolved X-ray diffractometry in the Collective Use Center of the Siberian Synchrotron and Terahertz Radiation Center (CUC SSTRC) based on the Budker Institute of Nuclear Physics Siberian Branch of the Russian Academy of Sciences (BINP).

The following were obtained for the first time by *in situ* X-ray diffractometry with SR at the SSTRC:

- a temporal resolution of 1 ms for SR diffraction experiments in the investigation of self-propagating high-temperature synthesis (SHS);
- information about chemical transformation kinetics in the nickel–aluminum reaction zone;
- a time resolution of 125 ns for a 1 ns exposure for the investigation of detonation and shock-wave processes by small-angle X-ray scattering (SAXS) of SR;
- information about the formation dynamics of the nanoparticles of silver, nickel, lead, and bismuth from their carboxylates under shock-wave loading;
- information about the formation dynamics of diamond nanoparticles in their detonation synthesis from a trinitrotoluene–hexogen system and the spatial distribution of the nanodiamond nucleation zone.

### 1.1 Historical reference

The historically first mention of SR supposedly is that of the Crab Nebula glow, originating from a supernova that was described by Japanese and Chinese monks in the chronicles of 1054, 900 years prior to the advent of synchrotrons. ‘Human-made’ SR was first observed in the USA at the General Electric synchrotron in 1947, and later at Soviet synchrotrons at the Lebedev Physical Institute. Strictly speaking, SR is the radiation of relativistic electrons in a magnetic field (in the case of the Crab Nebula, in the interstellar magnetic field), and it received the name synchrotron radiation in honor of the facility at which it was first observed.

The active proponents and inspirers of the development of SR research in the Institute of Nuclear Physics of the Siberian Branch of the USSR Academy of Sciences (INP) (presently the Budker Institute of Nuclear Physics, Siberian Branch of the Russian Academy of Sciences, BINP) were its first director G I Budker and A N Skrinskii. They also participated directly in a number of studies.

The first ten years of work with SR at the INP saw a sharp increase in the number of experimental groups using this radiation in the USSR and abroad (from 5 groups in 1975 to 87 in 1984), a rapid broadening of the field of work with SR beams, both for research and technological purposes, and the formation of a proficient community of SR users.

Researchers needed more SR beams than could be provided by the INP storage rings, which were initially made for high-energy physics. The requirements imposed on SR beams would also become more stringent. That is why a start was made worldwide on the development and construction of dedicated storage rings as SR sources, including the INP, which made the ‘Sibir’ storage ring for the Institute of Atomic Energy (Moscow) and the Zelenograd technological storage complex of the Lukin Research Institute of Physical Problems (Moscow region). The INP has made a substantial contribution to the development of SR sources throughout the world, and the institutes of the Siberian Branch of the Russian Academy of Sciences have made a contribution to the development of its application to

chemistry, catalysis, biology, geology, and material science problems.

Theoretical work has suggested that the SR produced by ultrarelativistic particles in cyclic accelerators must have extraordinary properties: a high intensity, which exceeds the intensity of traditional radiation sources in the vacuum ultraviolet (VUV), soft, and hard X-ray spectral regions by several orders of magnitude; a continuous (‘white’) spectrum; a low angular beam divergence; a high polarization degree; and a deterministic temporal structure. Due to these properties, vivid interest in the use of SR to solve various scientific problems took shape in the world in the 1950s–1970s. At that time, the actual sources of SR were the synchrotrons constructed and under construction for high-energy physics and nuclear physics. Since the late 1950s, several synchrotrons have been equipped with special channels for the extraction of SR, primarily for VUV spectroscopy.

The next stage, which stimulated the use of SR even more, was the development in the 1960s of synchrotron variations—storage rings for ultrarelativistic charged particle beams. Particle beams, which are injected and accelerated to a very high energy, continue to circulate with a constant energy for several dozen hours owing to the ultra-high vacuum in the storage rings. This strongly increases the average particle current in the storage ring and hence the average SR flux, thereby making the SR beam available at any time (and not only at certain moments, as in synchrotron acceleration cycles). A unique situation formed in the USSR: practically all storage rings were located at the INP in Novosibirsk.

The INP was one of the world’s pioneers of the counter-propagating beam technique. Under Budker’s supervision, the first electron–electron collider, VEP-1 (160 MeV), was made at the INP in 1963, followed by an electron–positron collider, VEPP-2 (670 MeV, 1967). Subsequently, an electron–positron collider, VEPP-3, was commissioned (2 GeV, 1973), and VEPP-2 was replaced by a new collider, VEPP-2M (670 MeV), which was operational starting in 1974. The SR spectrum of these storage rings covered the entire range from UV radiation to hard X-rays.

### 1.2 Onset and progress of work to use synchrotron radiation in Novosibirsk

In view of the growing interest in the use of synchrotron radiation in the world, in December 1972, a decision was taken to make a channel for extracting the X-ray part of the SR from the recently commissioned VEPP-3 storage ring (particle energy up to 2.2 GeV). In July 1973, the first SR extraction channel was constructed and the X-ray beam was extracted into the atmosphere in the experimental hall of the VEPP-3 storage ring [1, 2].

That same year, M A Mokul’skii’s group from the biological department of the Kurchatov Institute of Atomic Energy (Moscow) obtained the first diffractograms of sodium and cesium salts of DNA using the extracted X-ray SR beam from VEPP-3 [3]. The next year, in 1974, the group of A A Vazina from the Institute of Biophysics of the USSR Academy of Sciences (Pushchino) began investigations of long-period biopolymers, in particular, the muscle structure. Using an OD-1 one-coordinate X-ray detector developed at INP, an X-ray diffraction ‘movie’ method was developed, initially with a 100-millisecond time resolution and later on with a two-millisecond resolution [4]. The English scientists

who were using an X-ray tube spent 2 hours to obtain the same information about the muscle structure. Subsequently, as a result of many years of systematic research into muscle contraction, Vazina's group managed to construct a structural model of a muscle and its contraction.

In 1974, with the use of the dedicated diffractometer SID-1, Mokul'skii's group obtained the first SR diffractograms of a variety of samples with the X-ray SR beam extracted from VEPP-3 [1, 2]. The time required for recording diffraction patterns was shown to be significantly shorter (by about 50–100 times) than that required with the use of X-ray tubes (XRTs) (wavelength  $\lambda = 1.54 \text{ \AA}$ , Cu K $\alpha$ ), without the use of any focusing devices. Using the radiation with  $\lambda = 1.2 \text{ \AA}$ , i.e., a harder radiation than commonly employed, and thereby lowering absorption in the sample, the authors of Refs [3, 5] were able to obtain high-quality X-ray Cs DNA diffraction patterns of a calf's thymus gland and the Cs DNA diffraction patterns of a T2 phage on RT-1 photographic film in a time of the order of 1 h for a current of 30–40 mA in the storage ring. These X-ray patterns permitted determining the coordinates of atoms in the DNA [4].

In the late 1970s, considerable interest was expressed by material scientists and chemists in the application of SR to studies of changes in materials under the action of different factors or in the course of chemical reactions using X-ray diffraction movie techniques. These techniques were successfully developed and employed with the SR beams of VEPP-3 in different institutes, namely by B P Tolochko's group (Institute of Solid State Chemistry and Minerals Processing, Siberian Branch of the USSR Academy of Sciences) [6–8] for investigating solid-phase reactions, including self-propagating high-temperature synthesis; by B K Barakhtin et al. (Ioffe Physicotechnical Institute Academy of Sciences the USSR, Leningrad) for studying the dislocation structure dynamics in the course of metal deformation [9]; by P Forgacs (Institute of Plastics, Hungarian Academy of Sciences, Budapest, Hungary) for investigating phase transitions in plastic materials [10, 11]; by U Steinike (Central Institute of Physical Chemistry, Berlin, Germany) for investigating chemical processes in mechanoactivated materials [12, 13]; and by U Lembke (Rostock University, Germany) for the investigation of sol–gel processes [14].

## 2. Development of fast one-coordinate X-ray detectors at the BINP Physics

The one-coordinate OD-3M detector [15] is intended to carry out dynamic experiments to record small-angle scattering. The detector is based on the technology of a multiwire gas proportional chamber. The angular detector aperture is equal to  $13^\circ$  for a focal length of 1 m (the distance from the source of scattered radiation). The number of coordinate channels is  $\approx 3330$ , the channel spacing is  $\approx 70 \text{ }\mu\text{m}$ , and the spatial resolution for 8-keV photons (FWHM) is  $\approx 230 \text{ }\mu\text{m}$ , which corresponds to the angular resolution of about  $0.013^\circ$ .

A one-coordinate OD-4 detector is under development at the BINP. It is based on the technology of gas electron multipliers (GEMs) and is intended to carry out dynamic experiments to record large-angle powder diffraction patterns. The detector will permit recording radiation with an energy up to 10 keV with a spatial resolution of about 0.4 mm (FWHM), which corresponds to the angular resolution better than  $0.1^\circ$  for a focal distance of 35 cm. The angular aperture of the first detector version is  $67^\circ$  and the number of channels



Figure 1. One-coordinate X-ray DIMEX detector.

is equal to 2048. OD-4 operates in the direct X-ray photon counting mode.

A one-coordinate Detector for IMaging of EXplosions (DIMEX) was developed at the BINP for experiments in the observation of small-angle scattering and direct X-ray radiography of explosion processes (Fig. 1). A DIMEX version based on gas technology, DIMEX-G, now is in operation in VEPP-3 and VEPP-4M (VEPP is the acronym of the Russian for “Counterpropagating electron–positron beams”). DIMEX-G has 512 coordinate channels spaced at  $100 \text{ }\mu\text{m}$ . The measured spatial resolution is about  $200 \text{ }\mu\text{m}$  (FWHM) for 20 keV photons. Each detector channel can measure a signal corresponding to up to  $\sim 5000$  photons (20 keV) and record up to 100 measurements with a frame rate up to 8 MHz.

A new version of this detector, DIMEX-Si, is now under development, which relies on silicon microstrip detector technology. In the new detector, the dynamic range will be increased to  $10^6$  photons, the channel spacing (the spatial resolution) will be decreased to  $50 \text{ }\mu\text{m}$ , and the peak frame rate will be 50 MHz (20 ns between measurements). Furthermore, the new technology will permit making a two-coordinate detector, with a resolution of  $50 \text{ }\mu\text{m}$  in one coordinate and about 1 mm in the other [16].

## 3. Experimental stations of time-resolved diffractometry at the Siberian Synchrotron and Terahertz Radiation Center

### 3.1 Time-resolved experimental station ‘Diffraction movie’ in channel 5-b of the VEPP-3 storage ring

The work of staff members of the BINP and the Institute of Solid State Chemistry and Mechanochemistry (ISSCM), Siberian Branch of the Russian Academy of Sciences [17] describes the developed experimental facilities (experimental stations at SR channels), X-ray detectors, and the methods. In particular, a valid selection and design were made of: (i) the setup of the SR diffractometer ‘Diffraction movie’ in the 5-b channel of VEPP-3 (BINP) and (ii) the block diagram for recording X-ray diffraction patterns. Their realization permitted developing a technique for the investigation of fast structural substance changes. A series of X-ray diffraction patterns was recorded with a time resolution of 1 ms.

Experiments to investigate the kinetics of solid-phase reactions were performed at the ‘Diffraction movie’ station. The required wavelength adjustment was made with reference to the K absorption edge in nickel. The radiation is delivered to the station from a wiggler installed in VEPP-3. The configuration of the wiggler magnetic field determines the electron trajectory such that the radiation arrives at the

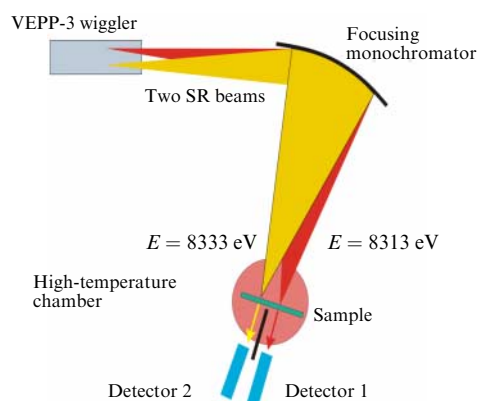


Figure 2. Layout of the two-beam anomalous scattering experiment.

station's monochromator from two points at different angles (Fig. 2), and therefore two beams of different energy are reflected from the monochromator. This setup made it possible to realize the method developed for two-beam anomalous scattering [18], in which two SR beams of different energy are simultaneously employed in the experiment. The use of a focusing monochromator permits separating the beams in space and working with each beam independently, and both beams turn out to be focused because their energy difference is small (18 eV).

The dispersion corrections to atomic scattering factors exhibit resonance changes near the K absorption edges: the real part of the correction decreases as the K edge is approached, while the imaginary part increases sharply at radiation energies above the absorption energy. The magnitude of this change depends on how close the wavelength is to the K absorption edge, the content of nickel in the phase under study, and the interference of the waves reflected from the nickel and other sublattices. To interpret the resultant intensity changes, the structural factors for different reflexes must be calculated. For this, the theoretical X-ray diffraction patterns for the two phases of nickel oxide,  $\alpha$ -NiMoO<sub>4</sub> and  $\beta$ -NiMoO<sub>4</sub>, were calculated.

To verify the method, a test experiment was performed to measure the intensities of reflexes from an NiO and MoO<sub>3</sub> mixture. The measured intensity difference for the (111) NiO reflex was 18%, and the reference reflex of MoO<sub>3</sub> intensity did not change (Fig. 3). The measured intensity difference for

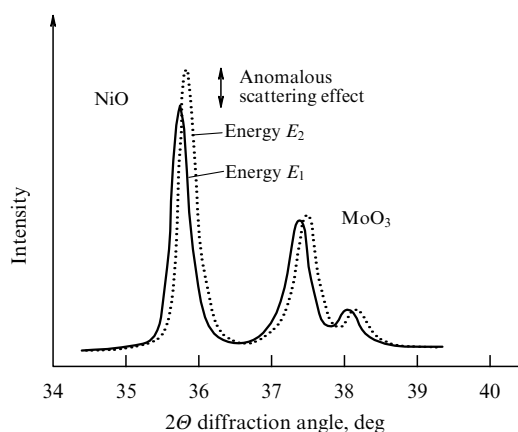


Figure 3. Test experiment on anomalous scattering in an NiO + MoO<sub>3</sub> sample mixture. The energy difference is  $E_1 - E_2 = 18$  eV.

the NiO reflex can be compared with the calculated one, which is equal to 15.5%.

### 3.2 'Explosion' station in channel 0-b of VEPP-3

To realize shock-wave experiments, staff members of the Lavrent'ev Institute of Hydrodynamics, Siberian Branch of the Russian Academy of Sciences, and ISSCM, Siberian Branch of the Russian Academy of Sciences [19–21] developed and implemented an experimental project of an 'Explosion' SR station on VEPP-3 (Fig. 4). This is a unique experimental facility, on which in 2000 on X-ray diffraction research was started on *in situ* processes in substances under the extreme conditions caused by the action of shock and detonation waves. For over 14 years, this was the world's only facility. In 2014, a similar one was commissioned at the Argonne National Laboratory (USA) at the Advanced Photon Source (APS) facility [22].

An exposure time of 1 ns at recording intervals of 125 ns was obtained with the station for shock-wave process research, with the number of frames equal to 32. The parameters of the high-speed experiment are defined by the temporal SR structure: on VEPP-3, the bunch duration is equal to 1 ns and the interbunch interval to 125 ns or 250 ns. The diffracted radiation has the same parameters.

The station consists of three main units: 1) the SR beam formation unit; 2) an explosion chamber; and 3) a recording unit. The recording unit comprises the SR beam formation unit, a vertical collimator (minimal aperture: 10  $\mu$ m; control step: 1  $\mu$ m), a horizontal collimator (minimal aperture: 100  $\mu$ m; control step: 10  $\mu$ m), a total reflection mirror, a filter unit, and a fast shutter. Placed in front of the entrance window is a fast electromagnetic shutter to protect the sample from exposure to high-intensity radiation. The shutter is opened on actuation of a trigger device. The explosion chamber can withstand an explosion with a trinitrotoluene equivalent of 50 g.

The experimental techniques implemented at the station with a nanosecond temporal resolution serve to (i) determine the three-dimensional substance density distribution in the axially symmetric case from the measurement data of a two-dimensional map of the X-ray absorption coefficient (Fig. 5); (ii) acquire data on the shock-wave compression of different substances [26, 27]; and (iii) investigate the dynamics of electron density fluctuations in a substance by the SAXS technique (Fig. 6).

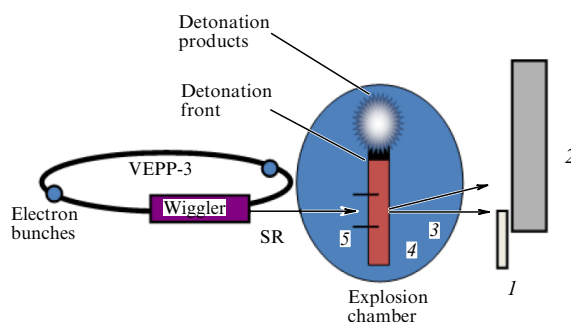
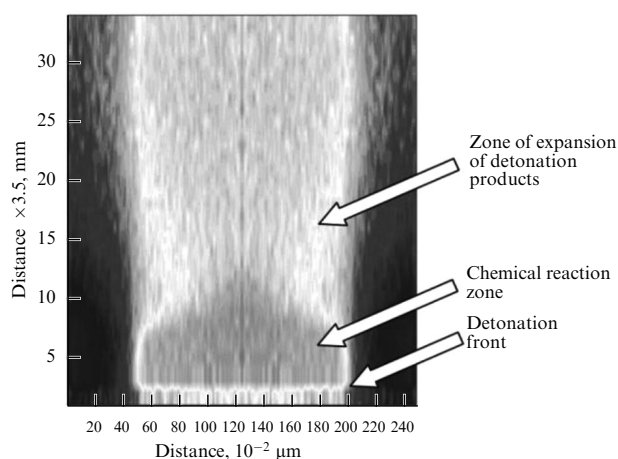
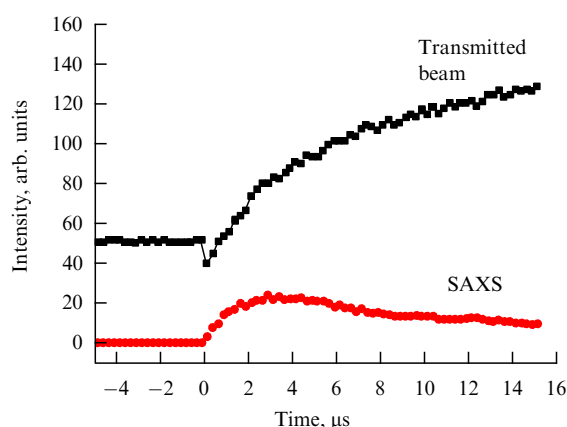


Figure 4. SAXS experiment for the investigation of detonation processes: 1—total radiation absorption detector, 2—one-coordinate DIMEX detector for recording the SAXS, 3—radiation scattered by a sample and transmitted through the sample, 4—high explosive, 5—contact detector for triggering the DIMEX detector.



**Figure 5.** (Color online.) Experimental data obtained using the one-dimensional DIMEX detector in the investigation of the density distribution behind the detonation front in the course of a trotyl–hexogen explosion. The color density in the drawing corresponds to different intensities of the SR beam transmitted through the sample.



**Figure 6.** Integral SAXS and trotyl-transmitted radiation intensities measured with a point-like germanium detector in the course of trotyl detonation.

### 3.3 ‘Precision diffractometry’ station in channel 6 of VEPP-3

The station constructed in SR extraction channel 6 of the VEPP-3 electron storage ring is intended for investigating the structure of and structural transformations in solids under different external conditions with the use of time-resolved X-ray diffraction techniques [28]. Experiments are carried out at the station with the use of monochromatic radiation with angular dispersion. The station comprises a monochromator, a radiation collimation system, a system for detecting the radiation diffracted by a sample, X-ray chambers in which different conditions can be realized for investigating a sample placed inside the chamber, and auxiliary equipment.

The primary ‘white’ SR beam is monochromatized by a single radiation reflection from a planar perfect crystal with a vertical deflection of the monochromatic beam by a fixed angle. The vertical deflection angle of the monochromatic SR beam from the median plane of the VEPP-3 storage ring, which is determined by the geometric station location (the beam has to pass through the ceiling of the first floor to reach the second level) is to about  $30^\circ$ .

The working radiation energy depends on the crystal type employed as a monochromator. Three crystal types are used at the station: Ge(111), Si(111), and Si(220). The selection of the working energy is governed by experimental conditions. Possible radiation energy values (wavelengths) are 7.162 keV (0.1731 nm) for the Ge(111) crystal, 7.460 keV (0.1662 nm) for Si(111), and 12.183 keV (0.10176 nm) for Si(220). The vertical beam size is limited by the diffractometer entrance slits  $\approx 0.1–0.2$  mm in width. Accordingly, the energy resolving power of the monochromator is  $\Delta E/E = \Delta\lambda/\lambda \sim 10^{-4}$ .

In the course of experiments, the X-ray diffraction patterns are recorded with a position-sensitive one-coordinate X-ray OD-3M-350 detector [29] developed and made at the BINP. The detector permits recording the diffracted radiation intensity simultaneously over an angular range of  $\approx 30^\circ$  with a discreteness of  $\approx 0.01^\circ$ . The detector design allows a microsecond time resolution, but the characteristic times of the processes under investigation do not require such a high operation speed, and the exposure time typically ranges from one to several dozen seconds per frame. The detector is mounted on a Huber 480 precision goniometer and can be positioned to the requisite  $2\theta$  diffraction angle determined by specific experimental conditions. Immediately before carrying out measurements, the detector is calibrated using the X-ray diffraction pattern of a standard corundum sample. The calibration procedure involves the determination of the correspondence between the detector channel number and the diffraction angle in the X-ray diffraction pattern. The calibration is performed for the detector position that is to be the working position for a specific experiment. The detector can be promptly moved to the requisite position by rotating the goniometer by a prescribed angle whenever needed.

The experimental station set comprises HTK-2000 and XRK-900 X-ray high-temperature chambers produced by Anton Paar (Austria). The HTK-2000 chamber is intended for X-ray diffraction studies on the structure and structural transformations in a sample under the action of a high temperature in the air, an inert medium, or a vacuum. The temperature ranges from room temperature to  $\sim 1300–1400^\circ\text{C}$  in the air and to  $2000^\circ\text{C}$  in a vacuum at pressures not lower than  $10^{-7}$  mbar.

### 3.4 ‘Hard X-ray diffractometry’ station in channel 4 of VEPP-3

The station is intended for *in situ* diffraction research with a temporal resolution in the hard X-ray energy range of SR [30]. The method used at the station is to pass a thin beam ( $0.4 \times 0.4$  mm) of monochromatic radiation ( $\lambda = 0.3686$  Å) through a sample layer to produce a diffraction pattern recorded with a planar two-dimensional detector. To record the diffracted radiation, a detection system based on the MAR345 memory screen produced by Marresearch is used. The X-rays incident on the screen are stored by the screen substance and can be read out by scanning the screen with a special device. Therefore, this detector can be considered to consist of  $9 \times 10^6$  pixels  $100 \times 100$  μm in size arranged in a circle 345 mm in diameter. This detection system has a broad dynamic range (from 1 to  $\approx 65,000$  intensity levels) and a high linearity of the resultant intensity values. The diffraction angle is calculated for all image elements from their pixel coordinates. Integrating the data over all directions allows obtaining the intensity as a function of the diffraction angle with a high statistical accuracy, even though the intensity per element can be low.



## 4. Time-resolved diffraction experiments at the Siberian Synchrotron and Terahertz Radiation Center

### 4.1 Self-propagating high-temperature synthesis

Self-propagating high-temperature synthesis (SHS) is among the promising methods of obtaining refractory compounds. The reaction is triggered with a powder charge and develops further due to the heat released in the reaction. The initial sample is a compressed pellet of a mixture of the powders of the initial components. When the reaction is initiated on one side of the sample, the reaction front travels through the sample at a speed ranging from several millimeters to several dozen meters per second (Fig. 7). The temperature in the reaction zone can range up to 5000 °C, which permits the synthesis of refractory compounds.

To date, the follows issues have been discussed in the literature: 1) does nickel interact with aluminum via a solid or liquid phase, considering that the melting temperature of Al is significantly lower than the reaction temperature; 2) are intermediate phases produced in the course of the reaction? The authors of Ref. [31] were the first to obtain experimental data on the development of SHS for a nickel–aluminum system with a time resolution of 5 ms and seem to have provided answers to these questions.

Considering the effects recorded during the reaction, the synthesis can be divided into four stages.

**First stage (0–20 ms).** An interesting experimental fact was discovered: in approaching the sample region under investigation (end face of the pellet irradiated by the SR beam), the intensity of nickel reflexes begins to decrease sharply, while the intensity of aluminum reflexes remains unchanged. Observed at the same time is a shift in nickel and aluminum reflexes to the smaller-angle domain, testifying to the rapid heating of the particles of the initial components.

It is noteworthy that the rate of aluminum heating at this stage is higher than that of nickel, and aluminum is therefore heated to a higher temperature than nickel. This process continues for 20 ms, with 14% of the nickel spent during this period. The reflexes of reaction products are not observed, and it is conceivable that nickel diffuses actively into the strongly heated aluminum to form a solid solution.

**Second stage (20–45 ms).** Early in the second stage, the aluminum reflexes begin to sink. By the end of this stage, the reflex intensity vanishes completely. During this period, the intensity of nickel reflexes decreases by 40%. Reflexes of a NiAl reaction product appear. The total increase in the

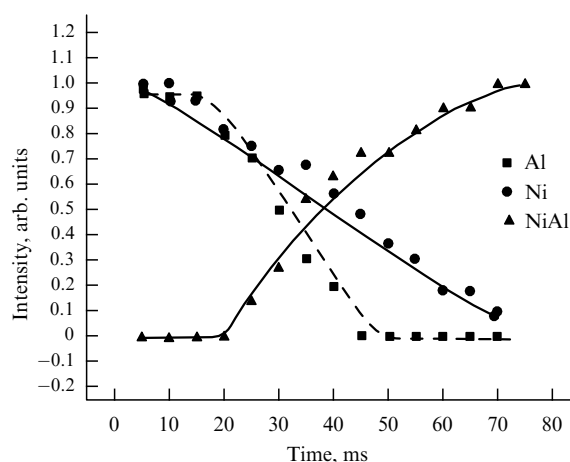


**Figure 8.** Dynamics of phase transitions in the zone of a Ni + Al system burning for 70 ms.

product reflex intensity amounts to 50% of the final reflex intensity (upon completion of the reaction). Observed in the middle of the stage is a sharp increase in the background intensity, which testifies to the onset of aluminum melting.

**Third stage (45–70 ms).** Aluminum reflexes are no longer present and nickel reflexes decrease to their complete disappearance. The intensity of nickel monoaluminum reflexes increases and reaches its maximum. Most likely, at this stage, the solid particles of nickel interact with molten aluminum. The intensity of nickel reflexes amounts to 46% of the initial intensity. The diffuse background continues to grow (Fig. 8).

**Fourth stage (70–70,000 ms).** The reflex intensities of the initial reagents are no longer present. The intensity of the final product is invariable in time. The Debye rings of the X-ray diffraction pattern disintegrate into separate reflexes of individual crystallites, which is an indication that recrystallization is in progress. These reflexes increase in intensity. At the same time, the crystallites grow, as is demonstrated by the geometric growth in the reflex areas. The diffuse background sinks and almost completely vanishes.

**Conclusion:** the state-of-the-art technology of SR beams allows investigating the variation of substance structure during SHS with a temporal resolution of about 5 ms and obtaining radically new, previously inaccessible information about the kinetics of the chemical reaction and about the emergence or absence of intermediate phases [32–36].

### 4.2 Detonation and shock-wave action

**Synthesis of diamonds from organic compounds.** The emergence of SAXS signals is observed not only in the detonation but also in the passage of high-power shock waves in organic substances. In the latter case, the shock wave provides a high pressure as well as strong heating sufficient for a deep disintegration of the initial organics. The motivation for research in this area was the discovery of a diamond phase in mixtures of high explosives (HEs) with organic materials (benzene, acetone, paraffin, hexane, and ethanol) and graphite [37].

A certain interest in the investigation of shock compression is due to the possibility of comparing HEs with ordinary (nonexplosive) carbon-rich compounds and with those HEs whose normal detonation is impossible under experimental conditions because of extremely large critical diameters.

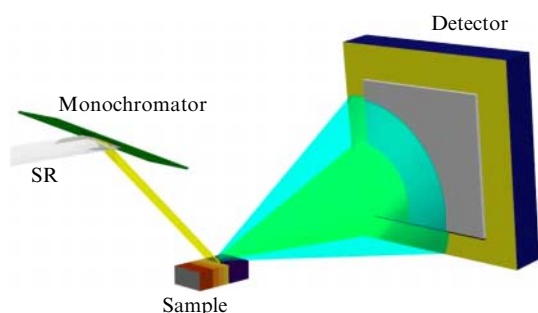


**Figure 7.** Schematic of an SHS experiment with the use of a two-coordinate DED-4 detector.

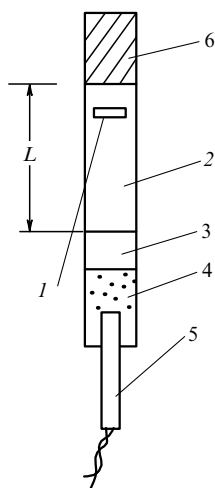


**Figure 9.** General view of experimental charge assembly: 1—target location for an SR beam, 2—substance under investigation, 3—octogen tablet, 4—octogen filling 5—detonator, 6—massive obstacle (shock wave reflector).

On the other hand, the investigation of the formation mechanism of free carbon and its condensation may shed light on the physics of several phenomena in shock-wave and detonation processes.

A schematic of an experimental charge assembly is shown in Fig. 9. Variations in the SR beam intensity transmitted through the shock-compressed substance and the magnitude of SAXS were measured in experiments. In some experiments, the SAXS signal was recorded by two detectors in two spectral regions. A silicon detector recorded the ‘soft’ component (approximately 7–15 keV) and a germanium detector recorded the ‘hard’ one (15–30 keV).

In the experiment preparation, the material under investigation was moulded in the form of a stub 12 mm high on a pressed (to a density of  $1.64 \text{ g cm}^{-3}$ , unless otherwise stated) blasting cartridge 12 mm in height and 12.5 mm in diameter, made of an HE of octogen or hexogen. The cartridge of pressed HE was initiated with a high-voltage detonator through a poured octogen charge.

To enhance the compression and moderate the unloading, an obstacle was fused to the stub of the material under investigation to form a secondary (reflected) shock wave. The obstacle was a brass cylinder 25 mm long with a base 12.5 mm in diameter.

The X-ray beam that passed through the middle of the stub of the substance under investigation, was recorded with a direct beam detector; SAXS detectors were located above and below it at angles of  $\approx 10^{-3}$  rad.

The data of density measurements from intensity variations in the X-ray SR beam transmitted through the shock-compressed substance and from the intensity of SAXS produced by particles of the high-density condensed phase are given in [37]. Several aromatic compounds with different numbers of nitrogen groups in the molecule were selected as the media for compression: naphthalene, isomeric mixtures of mono-, di-, and trinitronaphthalene, dinitrotoluene, and dinitrobenzene. Among these, naphthalene and its mononitro derivatives are not HEs, while the remaining compounds are weak explosives with large critical diameters. Furthermore, experiments on pressed samples of picric acid, nitroguanidine, and a polytetrafluoroethylene–aluminum

(27% Al) mixture were performed under the same conditions. In addition, shock compression of purified ultradispersed diamond powder and of a similar powder wetted with water was investigated.

To synthesize nanodiamonds, precursors were used: adamantane, stearic acid, carboxylates of metals, and trinitrotoluene (TNT), a precursor traditionally employed for the synthesis of nanodiamonds.

#### 4.3 Detonation nanodiamond synthesis from high explosives with a negative oxygen balance

With the use of trotyl as a shock-wave precursor (50/50 trotyl–hexogen system in the cylindrical charge), a high-intensity signal was observed in the small-angle domain [38].

An SAXS signal also appears in the TNT detonation without additions of hexogen. The SAXS signal begins to rise during compression in the detonation wave, when the SR beam illuminates the chemical reaction zone, and continues for about  $2 \mu\text{s}$ . The decay lasts for several hundred microseconds. The maximum SAXS signal intensity is 2–3 times stronger than the signal from the final product (a fusion mixture).

The authors of Ref. [38] believe that the SAXS in the detonation of the HEs in use is due to condensed carbon particles. This is confirmed by the increase in SAXS with an increase in negative oxygen balance of individual HEs. For the HEs investigated, the strongest SAXS signals correlate well with the yield of ultradispersed diamonds from these HEs.

Test experiments were made with plane charges of a 50/50 trotyl–hexogen (TH) mixture. Under these experimental conditions, the number of particles  $N$  first remains invariable because the SR beam encounters a plane detonation wave and not a cylindrical one, as in the above experiments. The SAXS signal nevertheless increases for  $\approx 2 \mu\text{s}$ .

The use of a DIMEX detector allowed obtaining information about the angular distribution of small-angle scattering with an exposure time of 1 ns. Processing a series of SAXS curves recorded during detonation at intervals of 250 ns permitted acquiring information on the dynamics of nanoparticle growth. It was found that the average size of diamond nanoparticles increases from 50 to 80 Å over  $4 \mu\text{s}$  [39].

A three-dimensional model was constructed assuming the existence of a zone with the most intense production of diamond nanoparticles. Additional experiments were carried out to verify the proposed model, and they confirmed its main propositions [40–42].

#### 4.4 Behavior of nanodiamonds artificially introduced into a detonation wave

The powder of nanodiamonds (NDs) was subjected to a shock wave with the same parameters as the detonation front in a 50/50 TH charge, the main composition for obtaining NDs. The experiment was performed in different media: in the air, water, and benzene. The ND powder was also impressed in different HEs. The SAXS signal was recorded simultaneously with the intensity of SR beam transmitted through the sample.

When the experiment was performed in the atmosphere, the X-ray scattering from nanodiamonds decreased drastically (to zero) at the instant they experienced the shock wave. It is likely that the NDs experience a huge pressure and temperature, resulting in a chemical interaction with the air (burning). When the shock wave acts on the NDs residing in the air, the SAXS signal remains unchanged and, accordingly, the NDs also remain unchanged.

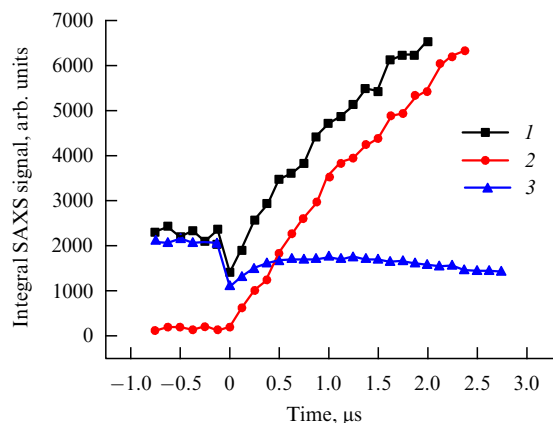


**Figure 10.** Time dependence of the integral SAXS signal in the detonation of charges of trinitrotoluene (curve 1) and hexogen (curve 3) with an 8% addition of ultradispersed diamonds, as well as of 50/50 TH (curve 2).

When ND particles were embedded in different HEs, the time dependence of the SAXS signal was different in different HEs (Fig. 10). In TNT, the SAXS signal increased, as in the case of pure trotyl. The time dependence of the SAXS signal for an ND/octogen mixture has a more complicated form: immediately after the detonation front, the signal amplitude decreases and then begins to increase. However, this increase is slower than in the 50/50 TH system, and 1  $\mu$ s later the signal begins to decrease again.

These experiments yield unique information about the behavior of NDs in the domain of their nucleation during detonation. This behavior is different in different media, including different HEs: in some HEs, nucleation is possible; in others, it is not. For instance, NDs burn out in octogen. Furthermore, it turns out that NDs can be used as oxygen sensors: NDs burn out when there is oxygen and persist when it is absent.

#### 4.5 Variation of hydrodynamic expansion conditions of detonation products as a tool to control the kinetics of nanodiamond growth

The assumption that the onset of ND crystal production occurs during unloading can be verified experimentally. In preparing the experiment, we took into account that the gasdynamic processes in detonation products (DPs) depend heavily on the DP expansion conditions: expansion in a vacuum occurs most rapidly, but when the HE is enclosed in a shell, the expansion is slower. The unloading rate also depends on the shell material. The DP unloading conditions are directly dependent on the expansion conditions. Consequently, by changing the shell material and its thickness, it is possible to control the unloading conditions and hence the kinetics of ND productions. This assumption was experimentally verified by the SAXS technique with the use of SR [43].

Implementation of this experiment requires that the shell material satisfy several requirements: 1) high transmittance to X-rays; 2) the absence of SAXS from this material during the action of the shock wave and during disruption and expansion; 3) the absence of toxic materials after the action of extreme detonation conditions; and 4) the relative cheapness of purchasing and fabrication. Beryllium ideally satisfies conditions 1 and 2 but does not satisfy conditions 3 and 4. After performing simulations and a series of test experiments, we decided in favor of polymethylmethacrylate (PMMA).

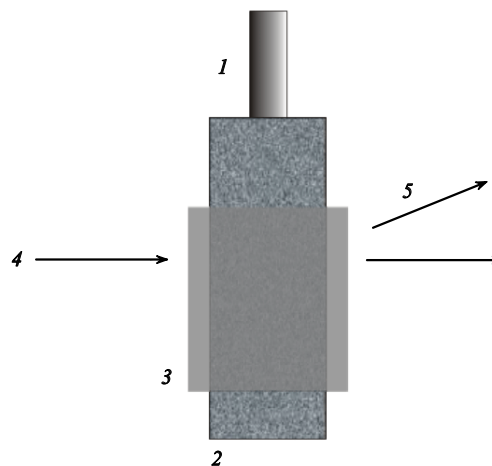


**Figure 11.** Schematic of the experiment to reveal the influence of hydrodynamic conditions of detonation product expansion on the kinetics of detonation ND production: 1—detonator, 2—explosive, 3—PMMA shell, 4—primary SR beam, 5—SAXS.

The experiment is schematized in Fig. 11. Three series of experiments were done with the use of 1.5, 3, and 6 mm shells. A 1:1 TNT–hexogen mixture was used as the HE.

As expected, adding a shell was experimentally found to substantially affect the dynamics of intensity  $I$  of the integral SAXS signal: a shell 1.5 mm thick decreases the derivative  $dI/dt$  from  $6000 \times 10^9$  pulses per second (shell-free HE) to  $3200 \times 10^9$  pulses per second, while the 3 and 6 mm shells respectively decrease it to  $2400 \times 10^9$  and  $1500 \times 10^9$  pulses per second (Fig. 12).

Because the shell placement results in an additional absorption of the primary SR beam and the SAXS radiation, the time dependence of the SAXS curves requires a correction. The absorption of 20 keV X-rays by 1.5, 3, and 6 mm shells respectively amounts to 10, 19, and 34%.

Thus, it was shown experimentally that the variation in the conditions of DP unloading (moderation) results in a variation in ND production conditions, specifically, in a moderation of the kinetics of this process.

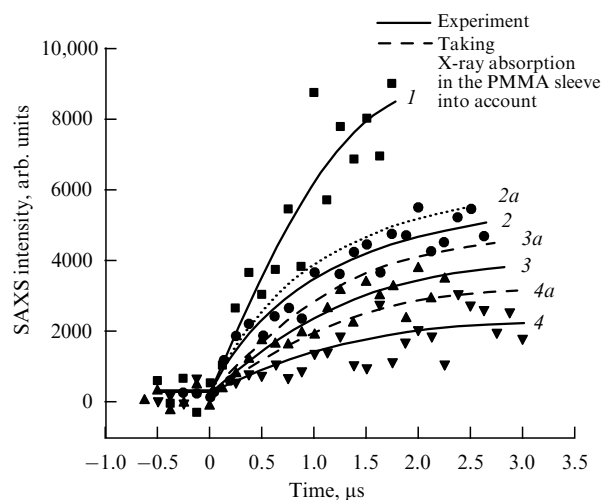


**Figure 12.** Behavior of the SAXS signal intensity during 50/50 TH detonation with the use of PMMA shells of various thicknesses: curve 1—without shell, curves 2 (2a), 3 (3a), and 4 (4a)—with shells 1.5 mm, 3 mm, and 6 mm in thickness.



By plotting the dependence of  $dI/dt$  on the shell thickness, it is possible to extrapolate the experimental curve to the domain of large sleeve thicknesses. The extrapolated curve intersects the abscissa at a value of about 15 mm. We can therefore conclude that for a shell thickness of about 15 mm, NDs are not produced in the region of SR beam passage. This formal conclusion has a specific physical explanation: adding the shell displaces the DP unloading front, and therefore the ND production region recedes from the detonation front by a distance comparable to the charge diameter.

Thus, in the investigation of ND synthesis, it was discovered that diamond nucleation slows down upon lengthening the reagent residence time under extreme conditions, although these physical conditions are more favorable for carbon to form the diamond structure. By varying the experimental conditions, it was possible to control the diamond nucleation rate over a wide range.

By extrapolating the resultant data, it was shown that the nucleation of diamonds can stop completely.

#### 4.6 Shock-wave synthesis of Ag, Bi, Co, and Pb nanoparticles

Experiments on the thermal decomposition of organic salts—Ar, Bi, Co, and Pb carboxylates—under the extreme conditions of high temperatures (up to 5000 °C) and pressures (300 kbar) are reported in [44]. The extreme conditions were produced in the shock-wave loading of these carboxylates. Information about nanoparticle production was obtained *in situ* with an SR beam using the SAXS method with a nanosecond temporal resolution.

It was discovered that several nanoseconds after the shock-wave action on the carboxylates, SAXS appeared from the nanoparticles produced in the decomposition of the carboxylates. The production of metal nanoparticles lasted for several microseconds.

The scorching metal particles were expected to oxidize in contact with the air during the first microseconds of expansion. Surprisingly, this did not occur: the SAXS signal did not decrease with time (up to 14  $\mu$ s), unlike that in the formation of diamond in the TH system, where the signal would begin to decrease in 3  $\mu$ s.

An analysis of carboxylate decomposition products by X-ray diffraction and electron microscopy techniques confirmed that metal (Ag, Bi, Co, Pb) nanoparticles formed. An interesting fact was discovered simultaneously: the metal nanoparticles in the decomposition product are perfectly spherical in shape and are covered with a thin layer (about 20 Å) of amorphous carbon. The existence of an amorphous protective coating of the metal nanoparticles explains the nontrivial behavior of the SAXS signal during the shock-wave action: these nanoparticles do not interact with gases, do not diminish in size, and do not vanish.

It was also discovered that the conductivity of carboxylates increases by two orders of magnitude during the action of a shock wave. This conduction was found to be electronic. This fact is also an indication that active reduction processes occur in carboxylates, which is attended by intense transfer of electrons and ions.

The characteristic size of the nanoparticles obtained from silver stearate (AgSt) is about 30–200 Å. Similar results were obtained in the action of a shock wave on bismuth, cobalt, iron, and lead stearates. The shock wave action on zinc stearate resulted in the formation of ultradispersed zinc oxide (ZnO). A physico-chemical model was constructed to

describe the production of metallic nanoparticles and ultra-dispersed diamonds for metal carboxylates under the action of a shock wave.

The authors of [44] believe that the formation of metallic nanoparticles in a characteristic time  $\tau_r$  requires a high substance density for a high mobility of the metal-bearing compounds of which the nanoparticles are formed. The high mobility in a dense material (the HE density is about  $1.6 \times 10^3 \text{ kg m}^{-3}$ ) is provided by the high temperature of the reaction mixture ( $T \sim 2000 \text{ K}$ ). The metallic clusters should grow by a diffusion mechanism. The resultant diffusion coefficient  $D \sim 10^{-10} \text{ m}^2 \text{ s}^{-1}$  is close to the diffusion coefficient in a liquid:  $D_{\text{liq}} \sim 10^{-9} \text{ m}^2 \text{ s}^{-1}$ . The properties of the medium in which metallic particles are produced are therefore closer to the properties of a liquid substance state than to those of a solid or gaseous state.

#### 4.7 Phase transitions in the course of preparation and activation of Co–Al catalysts for Fischer–Tropsch synthesis

Researchers at the Boreskov Institute of Catalysis, Siberian Branch of the Russian Academy of Sciences studied three samples synthesized under various conditions [45]. Sample No. 1 was obtained by the coprecipitation of Co and Al cations from nitrate salts with a solution of soda. The initial reagent compositions were selected so as to provide the Co:Al = 1:1 cation ratio in the precipitated product. Samples No. 2 and No. 3 were synthesized by precipitation from a solution of cobalt nitrate under conditions of hydrolysis of carbamide to  $\delta$  and  $\gamma$   $\text{Al}_2\text{O}_3$ . The amount of cobalt introduced into samples No. 2 and No. 3 was respectively equal to 15.9 and 19.9 weight %.

The dynamics of phase composition and structure variations in the precursor compounds of Co–Al catalysts during thermal processing and subsequent activation was investigated using different physico-chemical methods, including X-ray diffraction, *in situ* with the use of SR.

In the diffraction experiments, the samples were placed in a high-temperature X-ray reactor chamber, the flow of the gas mixture was turned on, the heating was turned on, and X-ray patterns were recorded in the course of heating. To preliminarily process the samples, an inert gas was let into the chamber in one case and a mixture of the inert gas with 3 volume % of NO in the other case. In the course of preliminary processing, the temperature growth rate was varied between 3 and 5 °C per minute and the gas mixture flow rate was 1.0–1.5  $\text{ml s}^{-1}$ . After preliminary processing with heating to 250 °C and subsequent cooling, a reduction was made in the flow of pure hydrogen with a rate of 1.0–1.5  $\text{ml s}^{-1}$  under heating at a rate of 2 °C  $\text{min}^{-1}$  at different temperature values.

Experiments on sample No. 3 ((Co, Al)/ $\gamma$ - $\text{Al}_2\text{O}_3$ ) were done with a special mode of increasing the temperature. In the course of activation, the heating was performed at a rate of no higher than 2 °C  $\text{min}^{-1}$ , and reduction in the flow of pure hydrogen occurred at a heating rate of 1 °C  $\text{min}^{-1}$  with an exposure under isothermal conditions at temperatures of 500 °C and 580 °C for 30 min.

All X-ray patterns of the samples in the initial state clearly show the reflexes characteristic of the hydrotalcite structure. Observed in the course of thermal precursor processing in the inert medium was the appearance of the products of cobalt–aluminum hydroxide–nitrate–carbonate thermal decomposition to nitrate–carbonate and then to the oxide with the

structure of a cobalt–aluminum spinel. In the Ar + 3% NO medium, now at a low temperature (about 50 °C), the reflexes shift to smaller angles, which is supposedly caused by the implantation of NO into the layered hydrotalcite structure. Subsequently, as in the previous case, the precursor disintegrates into cobalt–aluminum oxide via the nitrate–carbonate phase.

The following results were obtained in the course of the *in situ* investigation of the Co–Al catalysts of the Fischer–Tropsch process: 1) the sequence of phase transitions was determined for cobalt–aluminum hydroxide–nitrate–carbonate compounds of a hydrotalcite structure, which occur in their thermal processing (activation) and the subsequent reduction with hydrogen; the phase composition variations of the catalyst were revealed at all stages of its activation and reduction; the CoO particles resulting from the reduction have a microdomain structure, which consists of approximately 90% of the cobalt phase with a face-centered cubic (fcc) structure ( $\beta$ -Co) and 10% of the hexagonal close-packed (hcp) phase ( $\alpha$ -Co) [45]; 2) the final size of metallic cobalt particles depends primarily on the temperature growth rate in the activation of the precursor and its reduction: a slow heating entails a decrease in the size of metal particles, irrespective of the way the preliminary precursor is activated.

#### 4.8 Phase composition and structural transformations in strontium cobaltite ceramics under heating in different conditions

Iron-doped strontium cobaltites have a high oxygen conductance and are a good basis for making oxygen conducting membranes. The tolerance of a perovskite-type structure, which is typical for strontium cobaltites, to substitutions in the cation sublattice permit doping the structure with different cations and accordingly modifying the properties of the initial compound, including the ion–electron conduction. From the standpoint of practical applications, the material should be structurally stable under high-temperature conditions (800–900 °C) and low partial oxygen pressures ( $P(\text{O}_2) \sim 10^{-4} - 2 \times 10^{-1}$  bar) with a possible insignificant loss of oxygen conductance. The nonisovalent doping of  $\text{SrCo}_{0.8}\text{Fe}_{0.2}\text{O}_{3-\delta}$  in position B of the perovskite-type structure with the niobium cation having a higher oxidation degree than cobalt would lead to some reduction in the release of oxygen from the structure at temperatures 20–1000 °C and partial oxygen pressures  $10^{-4} - 2 \times 10^{-1}$  bar, but would improve the stability of the cubic perovskite structure. Furthermore, there is evidence that the structure of strontium ferrites and cobaltites is stabilized by niobium doping. It is therefore of interest to reveal the relation of the structure and structural transformations in perovskite-like oxides of composition  $\text{SrCo}_{0.8-x}\text{Fe}_{0.2}\text{Nb}_x\text{O}_{3-\delta}$ ,  $x = 0, 0.1, 0.2, 0.3$ , which can occur under high temperatures and different partial oxygen pressures, to their oxygen conductance.

The main experimental method for solving this problem is the time-resolved X-ray diffraction of SR, which provides a detailed analysis of the structure and its variations under different conditions [46]. The use of SR made it possible to discover the following dynamic effects in oxygen-deficient perovskites  $\text{SrCo}_{0.8-x}\text{Fe}_{0.2}\text{Nb}_x\text{O}_{3-\delta}$  ( $x = 0, 0.1, 0.2, 0.3$ ) [47–50]:

- an increase in the niobium content leads to a decrease in oxygen loss and an increase in structural stability when heating the perovskites in a wide temperature range (20–1000 °C) in media with a different partial oxygen pressure.

The most stable oxygen conductance is observed for the composition  $\text{SrCo}_{0.6}\text{Fe}_{0.2}\text{Nb}_{0.2}\text{O}_{3-\delta}$ ;

- due to an isostructural phase transition under heating in a vacuum, an oxygen-deficient phase forms with a cubic perovskite structure and variable oxygen content. Observed in the temperature range 350–750 °C is the coexistence of the initial (with a constant or slightly temperature-dependent oxygen stoichiometry) and oxygen-deficient phases;

- only the oxygen-deficient phase of variable oxygen composition takes part in oxygen exchange with the gas phase.

#### 4.9 Interaction of gaseous hydrogen with metals

A research group at Tomsk State University obtained data about the formation kinetics of hydrogenic phases in palladium under electrolytic saturation with hydrogen and their decay at temperatures up to 200 °C [51]. The measurements were performed by time-resolved *in situ* diffractometry in the SR channel 6 of VEPP-3 [28]. The published data, which are required for assessing and improving the theoretical models of hydrogen subsystem formation and spatial hydrogen localization in metals, testify that the formation of hydrogenic phases in palladium begins simultaneously with the onset of electrolytic saturation and that they completely replace the metallic phase 90 minutes prior to the electrolytic saturation for a current density of 0.01 A m<sup>-2</sup> in the electrolytic cell. The hydrogenic phases decay upon heating to 150 °C.

#### 4.10 Lithium intercalation–deintercalation mechanism in nanodimensional cathode materials for lithium-ion batteries

The results of the investigation of cathode materials for lithium-ion batteries ( $\text{LiFe}_{1-x}\text{Mn}_x\text{PO}_4$ ) are published in [52]. The aim of the work was to use SR diffraction to study *in situ* the structural changes in the course of cycling of the composite nanodimensional cathode material  $\text{LiFePO}_4 - \text{Li}_3\text{V}_2(\text{PO}_4)_3$  (of a monoclinic structure) for determining the lithium intercalation–deintercalation mechanism. Unlike the  $\text{LiFePO}_4$  cycling curves, which are characterized by only one plateau at 3.4 V in the 3–4.3 V range corresponding to  $\text{Fe}^{2+} \rightarrow \text{Fe}^{3+}$  oxidation, the  $\text{Li}_3\text{V}_2(\text{PO}_4)_3$  cycling curves have three observable plateaus: at 3.6, 3.7, and 4.1 V, which corresponds to the  $\text{V}^{3+} \rightarrow \text{V}^{4+}$  oxidation and the structural transformation  $\text{Li}_3\text{V}_2(\text{PO}_4)_3 \rightarrow \text{Li}_{2.5}\text{V}_2(\text{PO}_4)_3 \rightarrow \text{Li}_2\text{V}_2(\text{PO}_4)_3 \rightarrow \text{LiV}_2(\text{PO}_4)_3$ .

The nanodimensional composite  $0.5\text{LiFePO}_4 - 0.5\text{Li}_3\text{V}_2(\text{PO}_4)_3$  prepared with the use of mechanical activation was investigated in [52]. According to X-ray phase analysis data, its diffraction pattern is a superposition of  $\text{LiFePO}_4$  and  $\text{Li}_3\text{V}_2(\text{PO}_4)_3$  reflexes. The composite was cycled in an electrochemical cell with an Li anode and an  $\text{LiPF}_6$ -based electrolyte. The charge curve of the composite clearly shows four plateaus, which correspond to  $\text{LiFePO}_4$  (the first plateau) and  $\text{Li}_3\text{V}_2(\text{PO}_4)_3$  (plateaus 2–4).

Figure 13 shows *in situ* SR diffraction data on the structural changes in the course of  $\text{LiFePO}_4 - \text{Li}_3\text{V}_2(\text{PO}_4)_3$  cycling. With reference to Fig. 13, in the region corresponding to the first plateau ( $\text{Fe}^{2+} \rightarrow \text{Fe}^{3+}$  oxidation), the  $\text{LiFePO}_4$  reflexes are hardly shifted, but some reflexes (for instance, 020 and 131) vanish. The  $\text{FePO}_4$  phase reflexes are not observed. Therefore, the single-phase mechanism of  $\text{LiFePO}_4$  deintercalation is most likely realized. In the  $\text{V}^{3+} \rightarrow \text{V}^{4+}$  oxidation region, initially (in the second plateau region) the

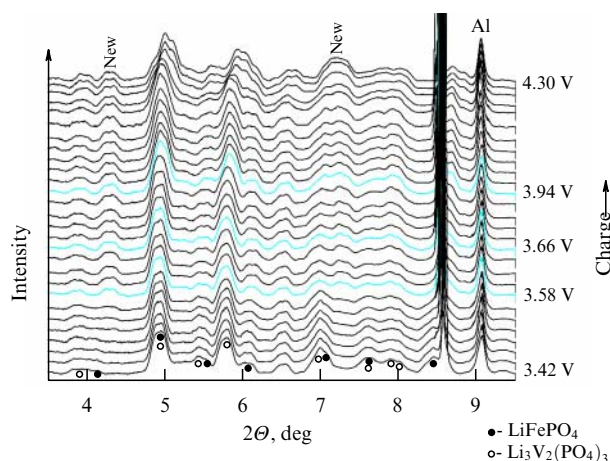


**Figure 13.** SR *in situ* diffraction by  $\text{LiFePO}_4/\text{Li}_3\text{V}_2(\text{PO}_4)_3$  in the course of electric cycling. The radiation wavelength is  $\lambda = 0.3685 \text{ \AA}$ . At a voltage higher than 4.11 V, the reflexes shift abruptly to larger angles and additional reflexes appear in the diffractograms at diffraction angles  $2\theta = 4.28^\circ$  and  $7.28^\circ$ .

$\text{Li}_3\text{V}_2(\text{PO}_4)_3$  reflexes gradually shift to the large angle domain, i.e., the lattice parameters of lithium–vanadium phosphate decrease slightly. The lattice parameters in the third plateau region remain practically invariable. For a voltage above 4.1 V, reflexes abruptly shift to larger angles, i.e., the lattice parameters become appreciably shorter. This corresponds to the earlier published data on  $\text{Li}_3\text{V}_2(\text{PO}_4)_3$ ,  $\text{Li}_{2.5}\text{V}_2(\text{PO}_4)_3$ ,  $\text{Li}_2\text{V}_2(\text{PO}_4)_3$ , and  $\text{LiV}_2(\text{PO}_4)_3$ . Furthermore, additional reflexes appear in the diffraction patterns at  $2\theta = 4.28^\circ$  and  $7.28^\circ$ .

#### 4.11 Processes at the electrolyte–solid electrode interface

Researchers at the ISSCM SB RAS [53] theoretically substantiated the feasibility of recording X-ray patterns from samples covered with a layer of electrolyte. This permitted selecting the conditions for the implementation of a method for obtaining structural information about the electrode and the electrochemical sediment directly during electrolysis.

The main problem with commercial X-ray tubes used in X-ray structure analysis, which hinders their use for investigating processes at the electrolyte–solution interface, is the limited spectral range of the radiation. Soft X-ray radiation is strongly scattered in the electrolyte, which hampers the passage of the primary as well as diffracted radiation through the electrolyte.

It was shown theoretically and confirmed experimentally that passing to the hard X-ray region — 30 keV and over — allows solving this problem. Solving the problem of radiation scattering in the electrolyte permitted investigating several processes occurring at the electrolyte–solid interface: 1) the rapid relaxation of deformed metallic electrodes, which are in contact with the electrolyte; 2) the saturation of nickel by hydrogen; and 3) the formation and decomposition of nickel hydride.

**4.11.1 Renewable electrode.** The same ISSCM SB RAS research group investigated the structure of mechanically renewed silver electrodes 0.4 s after renewing (cutting) [54]. The cutting was found to give rise to a thin (6–10  $\mu\text{m}$ ) deformed layer with a strongly distorted structure, the degree

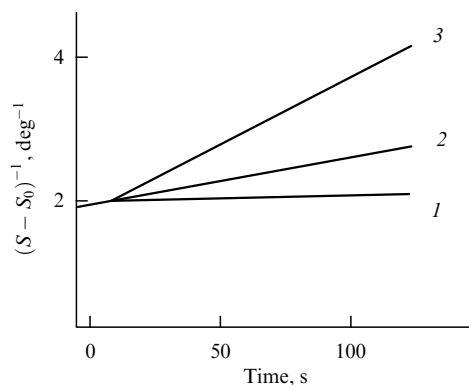


**Figure 14.** Relative change in the halfwidth  $S$  of the 111 reflex of silver after the cut-induced deformation at different temperatures: 1 —  $25^\circ\text{C}$ , 2 —  $80^\circ\text{C}$ , 3 —  $95^\circ\text{C}$ .  $S_0$  is the halfwidth for an annealed sample.

of distortion increasing closer to the surface. Information was obtained about the structural relaxation occurring in silver, copper, and nickel during the first seconds after the cut-induced deformation (Fig. 14). Kinetic measurements performed at different temperatures permitted determining the activation energy of these processes. Three time intervals were revealed in the time dependence of the relaxation process with different rates of structure variation.

**4.11.2 Formation of nickel hydrides.** The dynamics of crystal lattice variation for nickel hydride during electrolytic hydrogen saturation from the onset of nucleation to the point of stable phase development was investigated in [55].

It was found that the formation of the metastable phase of nickel hydride sets in practically simultaneously with the onset of nickel X-ray pattern variation: reflexes appear from the (111), (200), (220), (311), (222), and (400) planes. The reflexes of nickel hydride appear at smaller diffraction angles relative to the nickel reflex angles, because the lattice parameter of the new phase is 6% greater.

Figure 15 shows the growth dynamics of nickel hydride reflex intensities during cathodic hydrogen saturation. Early in the new phase formation, the nickel hydride reflexes are greatly broadened, which supposedly testifies to the small size of the nuclei of the new phase in the nickel matrix. In the course of hydrogen saturation, the nickel hydride nuclei grow: their size approaches 200  $\text{\AA}$ . It was simultaneously found that early in the new phase formation, the lattice parameter of nickel hydride differs from the lattice parameter of the initial metal by only 3% rather than the 6% measured after the completion of cathodic hydrogen saturation. In the course of hydride phase growth, the lattice parameter of nickel hydride increases and approaches 3.717  $\text{\AA}$ .

By analyzing the data on the variation in the nickel lattice parameter and the dynamics of nickel hydride formation (see Fig. 15), the authors of Ref. [55] concluded that the lattice parameter varied faster than the new phase was formed. This is an indication that hydrogen first penetrates the interstitial lattice sites to produce excess density there (it is known that the hydrogen density in the interstitial sites of the metal matrix is linearly related to the lattice parameter variation), and only then does the formation of nickel hydride begin. Specifically, in the first hydrogen saturation cycle, the hydrogen density in the matrix reaches 90% of its limit value

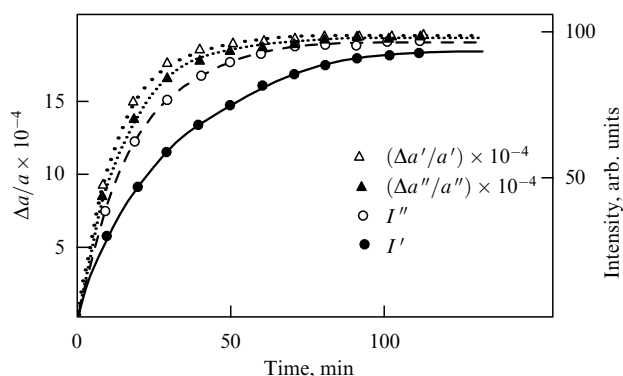


**Figure 15.** Experimental curves showing the nickel lattice parameter variation ( $\Delta a'$ : for the first hydrogen saturation,  $\Delta a''$ : for the second one) and the total intensity of the reflexes of nickel hydride in the course of its formation ( $I'$ : for the first hydrogen saturation cycle,  $I''$ : for the second one).

in 40 min, while that of nickel hydride amounts to only 69% of its limit value (see Fig. 15).

The growth and structural development of nickel hydride correlates in time with the development of the defect structure in the nickel matrix. The nickel crystal lattice is distorted most strongly at the initial stage of hydrogen saturation: lattice stacking faults of deformation type  $\alpha$  and of twinning type  $\beta$  appear, and the size  $\langle L \rangle$  of coherent scattering domains decreases.

#### 4.12 Synthesis of nickel tungstate

In [56], SR diffractometry was used to study *in situ* structural transformations during the reaction of nickel tungstate synthesis  $\text{NiO} + \text{WO}_3 \rightarrow \text{NiWO}_4$ . A qualitative phase analysis of the system was done in the course of solid phase interaction, and the time dependence of the content of nickel and tungsten oxides and nickel tungstate was estimated for systems with different relative contents of nickel and tungsten oxides.

The high intensity of SR provides a high time resolution, which made it possible to study the phase composition and structural changes occurring in the  $\text{NiO}/\text{WO}_3$  system, beginning with the first seconds of the reaction. The

following mixtures were taken as the initial sample for the synthesis of nickel tungstate:  $\text{NiO}(\text{WO}_3)_x$ ,  $x = 9, 2.33, 1.0, 0.43$ , and  $0.1$ . Prior to the investigation, the mixture was homogenized and mechanochemically activated in an AGO-2 ball planetary-type mill [57] for 15 s at a load of 40 g for all samples. The homogenized samples were placed in a high-temperature chamber installed at the 'Diffraction movie' experimental SR station [58].

During heating, it was possible to obtain data about the phase composition in the course of the reaction and about the kinetics of nickel tungstate formation (Fig. 16). The mixtures were annealed at temperatures of 540, 580, 640, and 720 °C. The time dependences of the intensities of the following reflexes were measured and processed: (200) of nickel oxide, (200) and (022) of tungsten oxide, and (111) and (020) of nickel tungstate. These reflexes were selected because their positions do not coincide with other reflexes.

The unique properties of SR permit gaining information about the onset of chemical transformations beginning with the first seconds of the synthesis: in the X-ray patterns, reflexes appear from the new-phase nuclei, which have a very low intensity in comparison with those of the initial reagents. The new-phase reflex intensities grow with time. The advantage of SR over X-ray tubes lies in the fact that SR provides the possibility in principle of recording the reflexes from a new phase existing in small quantities. While X-ray diffractometers permit recording a new-phase fraction of 1–5%, for SR this number is 0.01%. Another advantage offered by SR diffractometry is due to the narrow instrument function: a more exact determination of reflex positions allows a more precise determination of their shifts.

In experiments on the synthesis of nickel tungstate in Ref. [56], it was discovered that the new-phase nuclei emerging at the synthesis temperature of 720–740 °C exhibit stoichiometric composition, while the crystal lattice is not distorted and is identical in structure to nickel molybdate. The new phase nucleation at a lower temperature (580–640 °C) is attended by the formation of nuclei with a distorted structure: the composition is not stoichiometric, the lattice parameters are different from the tabulated values, and the reflexes are broadened. The structure of the nuclei evolves to the equilibrium structure with time.

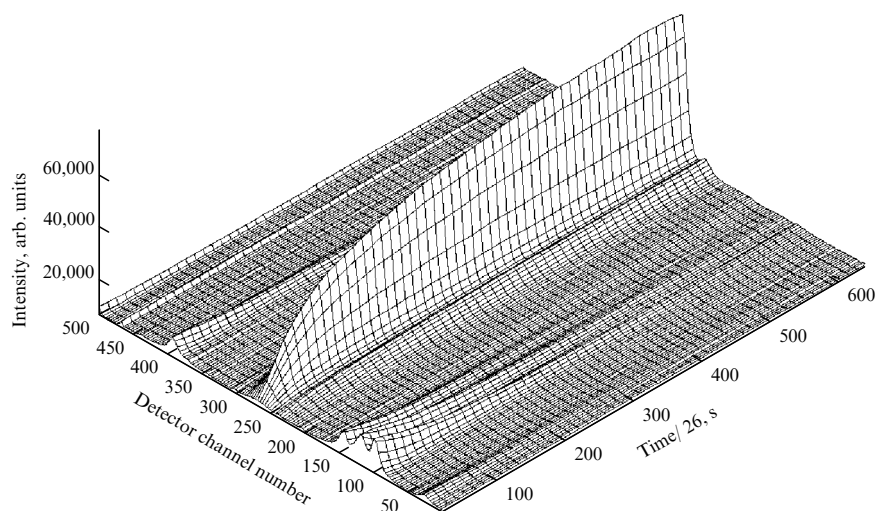


**Figure 16.** *In situ* investigation of the kinetics of the solid-phase synthesis of  $\text{NiWO}_4$  by SR X-ray diffraction. Dynamics of  $\text{NiO}$ ,  $\text{WO}_3$ , and  $\text{NiWO}_4$  X-ray pattern variations under isothermal heating at  $T = 650$  °C. One detector channel corresponds to 0.01 deg in  $2\theta$ .

The intensity of nickel tungstate reflexes increases sharply during the first several seconds of heating at all temperatures of synthesis (see Fig. 16). It is noteworthy that the halfwidth of nickel tungstate reflexes hardly changed during the first 500 s. This period is marked by the fastest variation of the lattice parameter: it rapidly approaches its equilibrium value.

Early in the reaction, X-ray diffraction patterns show only the first-order reflexes from the planes (011), (110), (111), etc., while the second-order reflexes from the same planes — (022), (220), (222) — are absent. This is an indication that the resultant nuclei are quite small in size and that the interference field of second-order reflexes cannot be formed.

At the onset of synthesis at a temperature of 540 °C, the (020) and (111) reflex intensity ratio is 1:4 and the ratio in the ideal nickel tungstate structure is 1:6. This testifies to a nonstoichiometric composition of the resultant nickel tungstate nuclei.

The broadening of reflexes for the diffractometer in use permits obtaining information about the grain size for particles 1000 Å in size and smaller. It was thus possible to investigate the growth of new-phase nuclei at the initial reaction stage. Broad reflexes, which are typical for small nickel tungstate particles, were observed only at the initial reaction stage (during the first 15 min of interaction). Subsequently, the width of nickel tungstate reflexes approached the instrumental width and decreased with time during synthesis.

It was found that the nucleation and growth of distorted new-phase nuclei at the points of contact of the reagents proceed in different ways at different temperatures. It is possible to conventionally mark out the 640 °C temperature: at higher temperatures, the nucleation and growth of distorted new-phase nuclei follow one pattern, while at temperatures below 640 °C they follow another one.

For  $T > 640$  °C, the new-phase nucleates during the first seconds of the reaction, as is suggested to by the emerging nickel tungstate reflexes (Fig. 16). However, their interplanar spacings exceed the tabulated values by 0.001 Å, which is an indication of lattice broadening, i.e., of a negative surface energy at the Ni/NiWO<sub>4</sub>/WO<sub>3</sub> interface. Furthermore, the reflexes are greatly broadened. The size of the nuclei formed at the onset of the reaction at different temperatures was determined from reflex broadening. It is to 310 Å at  $T = 720$  °C, 280 Å at  $T = 680$  °C, and 200 Å at  $T = 640$  °C.

For  $T < 640$  °C, the new-phase reflexes appear with some (temperature-dependent) delay after the beginning of synthesis. Observed at the same time are shifts in WO<sub>3</sub> reflexes, which testifies to the formation of a solid solution. The new-phase lattice parameters are 0.01 Å smaller than the tabulated values.

New-phase reflexes obtained at lower temperatures are significantly broader than the reflexes of the product obtained with a higher-temperature synthesis. This is suggestive of the formation of smaller nuclei and strong distortions of the lattice, pointing to the existence of microstress.

As the synthesis progresses with time, the reflex half-widths start to decrease rapidly, which is indicative of the growth in nuclei or of the weakening of microdistortions. The decrease follows an exponential law.

What is the reason for the structural difference between nuclei and the final product? There are several reasons:

— at the onset of the reaction, the nuclei of nickel tungstate contact only NiO and WO<sub>3</sub> particles, which naturally affects the crystal structure under formation;

— the molar volume of NiWO<sub>4</sub> is 10% smaller than the sum of the molar volumes of NiO and WO<sub>3</sub>. The incipient particles therefore experience tensile action of the surrounding matrix. Furthermore, the negative surface energy at the NiO/NiWO<sub>4</sub>/WO<sub>3</sub> interface also leads to tension in the nucleus. This effect weakens with the growth of the nuclei.

The kinetic curves were processed in the 0.2–0.8 transformation degree range using the Yander, Ginstling–Brounstein, Carter–Valensi, and other equations. Of all the models, we selected the one that provided the most adequate description of experimental data. After the formation of a thin product layer, i.e., for a transformation degree  $\alpha > 0.2$ , the time dependence of the intensity is satisfactorily described by the Ginstling–Brounstein curve.

#### 4.13 Synthesis of nickel molybdate

The study in [59] was motivated by the assumption that the layered MoO<sub>3</sub> structure should facilitate the diffusion of nickel oxide and that the authors of Refs [60, 61] might have made a mistake by neglecting this possibility. The aim of Ref. [59] was therefore to show, if possible, that in the synthesis of NiMoO<sub>4</sub>, at the diffusion stage nickel plays a role no less significant than molybdenum does, i.e., that their diffusion coefficients are comparable in magnitude.

To reach conformity with traditional models, first, in a special experiment at the stage of reaction mixture preparation, conditions were provided for the excessive presence of NiO particles around the  $\alpha$ -MoO<sub>3</sub> particles (mechanochemically homogenized mixtures with an excess of nickel oxide were taken in the ratio 10:1). Second, selective observation of the behavior of only the nickel atoms was organized (using the anomalous scattering effect [62] and the method of two-beam anomalous scattering [59], as well as extended X-ray absorption fine structure (EXAFS)), which permitted obtaining information about the crystallographic position of nickel in the resultant high-temperature phase of nickel molybdate  $\beta$ -NiMoO<sub>4</sub> and, as shown below, in the intermediate reaction phase.

It has been known [63] that the heating of  $\alpha$ -MoO<sub>3</sub> in a vacuum at a temperature of 608 °C is attended by a phase transition of molybdenum oxide to Mo<sub>4</sub>O<sub>11</sub>. However, in the annealing of  $\alpha$ -MoO<sub>3</sub> (without NiO) for an hour at a temperature of 650 °C in the experimental conditions of the ‘Diffraction movie’ station, as well as after sample cooling, the Mo<sub>4</sub>O<sub>11</sub> phase was not observed.

The heating of the same  $\alpha$ -MoO<sub>3</sub> in the presence of NiO led to the production of Mo<sub>4</sub>O<sub>11</sub>. This experiment has led to the conclusion that it is precisely the diffusion of nickel to molybdenum oxide that gives rise to the new phase Mo<sub>4</sub>O<sub>11</sub>. The fraction of nickel that underwent the reaction was only 20%, testifying to the fact that the resultant new phase Mo<sub>4</sub>O<sub>11</sub> forms a solid solution with NiO: Mo<sub>4</sub>O<sub>11</sub>/NiO.

The time dependence of the nickel oxide (200) reflex intensity shows two portions with different slopes: one with a steep slope and the other with a gentle one. The former portion corresponds in time to the formation of Mo<sub>4</sub>O<sub>11</sub>/NiO and a high nickel diffusion rate. The change in the slope in time coincides with the completion of new phase formation and is supposedly attributable to the change in the diffusion coefficient in the Mo<sub>4</sub>O<sub>11</sub>/NiO layer: in the new phase, the positions corresponding to nickel atoms are occupied, which strongly hampers the further diffusion of nickel. Doping NiO with lithium leads to a significant enhancement of the initial stages of the reaction of nickel molybdate synthesis.



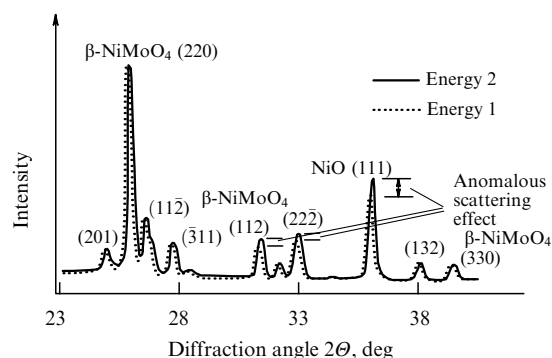


**Figure 17.** Two X-ray patterns obtained using the technique of two-beam anomalous scattering by the mixture  $0.25 \alpha\text{-MoO}_3 + \text{NiO}$  at a temperature of  $650^\circ\text{C}$ . The solid curve shows the X-ray pattern recorded away from the K absorption edge ( $\lambda = 1.49150 \text{ \AA}$ ), the dotted curve shows the X-ray pattern recorded near the K edge of nickel ( $\lambda = 1.48780 \text{ \AA}$ ) [59].

The further annealing of the system at a temperature of  $650^\circ\text{C}$  led to the formation of  $\beta\text{-NiMoO}_4$  (Fig. 17). Annealing at  $T = 690^\circ\text{C}$  also resulted in  $\text{NiMoO}_4$  formation. However, an amorphous halo appeared in this case, in addition to crystal phase reflexes (Fig. 18).

For the synthesis temperature of  $650^\circ\text{C}$ , good agreement with the data of numerical simulations was obtained for all experimentally observed reflexes (see Fig. 17). This suggests that nickel occupies the same positions in this structure as does Mn in the  $\alpha\text{-MnMoO}_4$  structure. For the synthesis temperature of  $690^\circ\text{C}$ , anomalous effects on  $\beta\text{-NiMoO}_4$  reflexes vanish for the same change in the nickel oxide (111) reflex intensity, and diffuse scattering increases markedly (Fig. 18). With the energy change from  $E_1$  to  $E_2$ , the intensity of diffuse scattering also changes, thereby indicating that this diffuse scattering is primarily produced by a disordered arrangement of nickel. These results suggest that nickel, for this synthesis temperature, occupies mainly interstitial positions. From the position of the diffuse peak, the distance between the nickel atoms residing in the interstitial sites is estimated as  $3 \text{ \AA}$ .

Diffuse scattering was therefore discovered to be highly sensitive to variations in the radiation energy in the vicinity of the nickel K absorption edge.

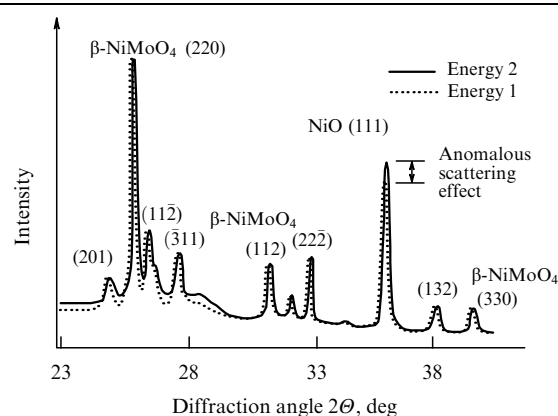


**Figure 18.** Two X-ray patterns obtained by two-beam anomalous scattering [25] with the mixture  $0.25 \alpha\text{-MoO}_3 + \text{NiO}$  at a temperature of  $690^\circ\text{C}$ . The solid curve shows the X-ray pattern recorded away from the K absorption edge ( $\lambda = 1.4934 \text{ \AA}$ ) and the dotted curve shows the X-ray pattern recorded near the K edge of nickel ( $\lambda = 1.4908 \text{ \AA}$ ) [59].

The effect of fast nickel consumption discovered for the initial stage of nickel molybdate synthesis permitted carrying out an experiment in which nickel oxide is completely used up and the system becomes monophasic. This is extremely important when using the EXAFS and X-ray absorption near-edge structure (XANES) methods. For this, the reagent  $\text{NiO} + \text{MoO}_3$  composition was taken in the ratio 1:10 in order to obtain a solid solution at a temperature of  $620^\circ\text{C}$ . The synthesis duration at  $T = 620^\circ\text{C}$  was selected such that the initial  $\text{NiO}$  was completely spent, and only one phase—the solid solution  $\text{Mo}_4\text{O}_{11}/\text{NiO}$ —remained in the system. At a temperature of about  $620^\circ\text{C}$ , the rapid formation of a new phase begins, which can be identified as  $\text{Mo}_4\text{O}_{11}$ . Its formation time is 18 min. On further annealing at a temperature of  $620^\circ\text{C}$  (after the new phase formation), the phase composition of the mixture remained invariable.

Therefore, it was shown that nickel diffuses into the crystal lattice of  $\text{MoO}_3$  in the solid-phase nickel molybdate synthesis from  $\text{NiO}$  and  $\text{MoO}_3$  and determines the reaction mechanism. When the mixture is heated to  $620^\circ\text{C}$ , vacancies are formed between layers of the octahedrons in the  $\text{MoO}_3$  structure, which destabilizes the molybdenum oxide structure and facilitates the diffusion of nickel atoms. All nickel that participates in the reaction  $0.1 \text{ NiO} + 1 \text{ MoO}_3$  diffuses into the interlayer space of  $\text{MoO}_3$  octahedrons and initiates the  $\alpha\text{-MoO}_3 \rightarrow \gamma\text{-Mo}_4\text{O}_{11}$  phase transition with the formation of the solid solution  $\gamma\text{-Mo}_4\text{O}_{11}/\text{NiO}$ .

The reaction diffusion of nickel in the  $\text{NiO} + \text{MoO}_3$  reaction proceeds in two stages. The first sees a rapid diffusion of 20% nickel, which is observed during the formation of a new  $\gamma\text{-Mo}_4\text{O}_{11}/\text{NiO}$  solid solution phase. The second involves a slow diffusion of the remaining nickel via the  $\gamma\text{-Mo}_4\text{O}_{11}/\text{NiO}$  solid solution phase. The formation of the final reaction product  $\beta\text{-NiMoO}_4$  occurs at this stage.

An experiment was performed to study the structure of the close environment of nickel atoms in the course of solid-phase synthesis with the use of the EXAFS technique. This technique allowed obtaining *in situ* information about the variation in the nickel environment in the course of the reaction. The EXAFS technique does not allow studying multiphase samples, and therefore a solid solution of  $\gamma\text{-Mo}_4\text{O}_{11}/\text{NiO}$  was preliminarily prepared for the experiment using the method described above.

XANES and EXAFS spectra were obtained in the fluorescence mode at the nickel K edge from a  $0.1 \text{ NiO} + \alpha\text{-MoO}_3$  powder mixture during its heating to  $620^\circ\text{C}$ . A model was constructed for the resultant structure, and its XANES and EXAFS spectra were calculated with this model. The *in situ* spectra were recorded in the course of heating at the EXAFS spectroscopy experimental station of VEPP-3 SSTRC at the BINP. The  $\text{NiO} + \alpha\text{-MoO}_3$  powder mixture in the ratio 0.1:1 was pressed in a copper cell placed on a heating element.

#### 4.14 Three-dimensional colloidal crystal formation

In [64], *in situ* SR diffractometry was used to experimentally determine the formation conditions for silver nanoparticles in the thermal decomposition of silver carboxylates. It was determined in [65] that the thermal decomposition of a series of carboxylates  $\text{C}_n\text{H}_{2n-1}\text{O}_2\text{Ag}$  ( $n = 6, 8, 10, 12, 14, 16, 18, 22$ ) gives rise to silver nanoparticles, which self-organize (self-assembly takes place) in a periodic structure, i.e., they form a three-dimensional colloidal crystal for  $n > 8$  (Fig. 19). This was confirmed experimentally using a transmission electron microscope.

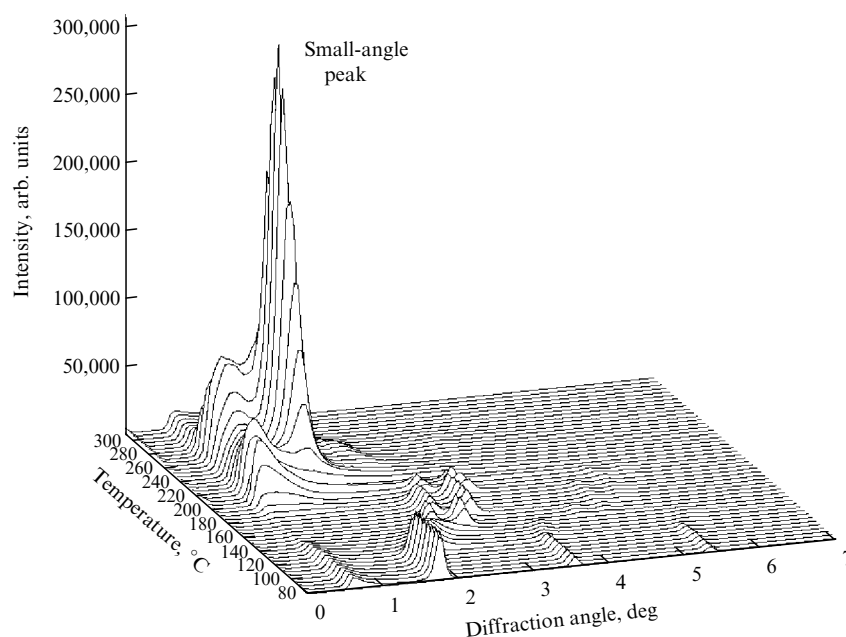


**Figure 19.** Diffractograms obtained in the course of silver stearate decomposition at different temperatures. The appearance of small-angle diffuse scattering at  $T = 220^\circ\text{C}$  is indicative of the formation of monodisperse silver particles. The emergence of a diffraction peak at  $T = 240^\circ\text{C}$  is indicative of the formation of an ordered structure of silver nanoparticles — a three-dimensional colloidal crystal.

The nanoparticle arrangement in the colloidal crystal was characteristic of hexagonal and cubic packings. The particles were approximately 60 Å in diameter and their central distance was about 80 Å. By comparing experimental data and simulations for nanoparticles 60 Å in diameter, arranged in an fcc structure with the cell parameter 98 Å, the choice was made in favor of the cubic structure.

One of the obvious prerequisites to the formation of a colloidal crystal is the monodisperseness of particles when they are of the same type. A narrow particle size distribution is the case where the production rate of nanoparticle nuclei is much higher than their growth rate. The growth rate might be limited by growth inhibitors, for instance, by molecules produced in the decomposition of carboxylates of the acid of the same name.

The nanoparticles resulting from the decomposition of carboxylates are surrounded by a protective coat of carboxylate decomposition products. When they were removed (in experiments with an open cell), silver nanoparticles immediately coagulated into a massive sample and colloidal crystals were not formed.

The temperature of the appearance of a small-angle peak was taken to be the temperature of ordered structure formation. Under the conditions of a closed system (a foil cavity) and a heating rate of  $10^\circ\text{C}$  per minute, the following temperature ranges were determined that allow the existence of an ordered structure:  $220\text{--}260^\circ\text{C}$  for behenate,  $225\text{--}275^\circ\text{C}$  for stearate,  $230\text{--}280^\circ\text{C}$  for palmitate,  $220\text{--}290^\circ\text{C}$  for myristate,  $220\text{--}280^\circ\text{C}$  for laurate, and  $240\text{--}290^\circ\text{C}$  for caprinate.

The imperfection of the three-dimensional colloidal crystal structure increases upon shortening the hydrocarbon chain length.

#### 4.15 Interaction dynamics of solid metals with liquid ones

The interaction of powder metals and alloys with liquid gallium eutectics underlies the formation of diffusion-hard-

ening alloys. Several phases, intermetallic and (or) metallic, can form simultaneously or sequentially in such multicomponent systems, affecting the kinetics of the process and the formation conditions for each other and, consequently, the resultant material properties.

The aim of Ref. [66] was to study the stages of the chemical interaction of solid metallic alloys with liquid metals and eutectics by X-ray structure analysis with the use of SR.

The sequence of phase formation in the chemical interaction of alloys in solid and liquid states has been determined.

The phase formation was shown to depend on which of the components in the interaction was in the solid state and which was liquid. This was shown by comparing the chemical interaction of the solid solution of tin in copper with the gallium–indium melt of eutectic composition and of the solid solution of indium in copper with the gallium–tin melt of eutectic composition, as well as of the copper–bismuth mechanical composition with these melts.

We list the main results:

1. Using *in situ* X-ray diffractometry, it was discovered that a  $\text{CuGa}_2$  intermetallide was formed in the room-temperature interaction in a copper–gallium binary system irrespective of the phase composition of the solid phase. It was found that other intermetallic phases were not formed [66].

2. In Cu–Ga–(In, Sn) ternary systems, the third component does not dissolve in the  $\text{CuGa}_2$  intermetallide. Instead it segregates in the form of a separate phase — a solid solution with gallium. The third component segregates in the form of a separate phase with a time delay. The growth dynamics of the solid solution phase testifies to the supersaturation of the liquid phase with tin or indium. The third component begins to segregate after a time inversely proportional to its concentration in the system [67].

3. According to a data analysis of the azimuthal distribution of reflex intensities, the  $\text{CuGa}_2$  intermetallide crystallite size is affected by the presence of the second segregated phase.

The crystallite size is inversely proportional to the concentration of the third component in the system [68].

4. The formation of the CuGa<sub>2</sub> intermetallide was observed in the interaction of the solid solution of tin in copper (20 mass. % Sn) with the gallium–indium melt of eutectic composition. Recorded 2.5 h later was the appearance of an intermediate phase: the solid solution of gallium in indium. The intermediate phase begins to disappear with time (5.5 h), and the In<sub>3</sub>Sn phase crystallization begins instead of it [69].

## 5. Conclusions

A powerful instrumentation complex has been developed in the Collective-Use Center of the SSTRC, intended primarily for the use by institutions of the Siberian Branch of the Russian Academy of Sciences. The instrumentation permits carrying out time-resolved X-ray diffraction experiments using SR.

Methods were developed and implemented for the first time in the world that make it possible to investigate the nucleation and growth dynamics of nanoparticles during explosions and shock-wave actions with nanosecond temporal resolution (X-ray pattern exposure time: 73 ps), to study the dynamics of structural transformations in the course of chemical reactions, to investigate the kinetics of chemical transformations during gas-free burning with a millisecond temporal resolution, to obtain structural information about the state of catalysts, and so on.

The SSTRC is developing, which permits the planning of new unique experiments by the institutions of the Siberian Branch of the Russian Academy of Sciences.

## Acknowledgements

This work was carried out in the Collective Use Center of the Siberian Synchrotron and Terahertz Radiation Center.

## References

- Mokul'skaya T D et al., Preprint IAE-2385 (Moscow: IAE, 1974)
- Mokul'skaya T D et al. *Dokl. Akad. Nauk SSSR* **218** 824 (1974)
- Mokul'skaya T D et al. *Kristallogr.* **22** 744 (1977)
- Vazina A A *Usp. Fiz. Nauk* **128** 182 (1979); *Sov. Phys. Usp.* **22** 385 (1979)
- Mokul'skii M A *Vestn. Akad. Nauk SSSR* **8** 8 (1978)
- Boldyrev V V et al. *Nucl. Instrum. Meth. Phys. Res. A* **261** 192 (1987)
- Aleksandrov V V, Korchagin M A, Tolochko B P, Sheromov M A *Combustion Explosion Shock Waves* **19** 430 (1983)
- Lyakhov N Z et al. *Nucl. Instrum. Meth. Phys. Res. A* **246** 776 (1986)
- Barahin B et al. *Nucl. Instrum. Meth. Phys. Res. A* **261** 223 (1987)
- Forgacs P et al. *J. Polymer Sci. Polymer Phys. Ed.* **18** 2155 (1980)
- Forgacs P, Sheromov M A, Tolochko B P *Polymer Bull.* **6** 127 (1981)
- Neissendorfer F, Steinike U, Tolochko B P, Sheromov M A *Nucl. Instrum. Meth. Phys. Res. A* **261** 216 (1987)
- Neissendorfer F, Steinike U, Tolochko B P, Sheromov M A *Nucl. Instrum. Meth. Phys. Res. A* **261** 219 (1987)
- Gaponov Yu A et al. *Nucl. Instrum. Meth. Phys. Res. A* **359** 170 (1995)
- Aulchenko V M et al. *Nucl. Instrum. Meth. Phys. Res. A* **603** 69 (2009)
- Aulchenko V et al. *Nucl. Instrum. Meth. Phys. Res. A* **845** 169 (2017)
- Evdokov O V, Titov V M, Tolochko B P, Sharafutdinov M R *Nucl. Instrum. Meth. Phys. Res. A* **603** 194 (2009)
- Bessergenev A V, Tolochko B P *Nucl. Instrum. Meth. Phys. Res. A* **359** 160 (1995)
- Aleshaev A N et al. *Nucl. Instrum. Meth. Phys. Res. A* **470** (1–2) 240 (2001)
- Aleshaev A N et al. *Fiz. Goreniya Vzryva* **37** (5) 104 (2001)
- Tolochko B P et al. *Nucl. Instrum. Meth. Phys. Res. A* **467–468** 990 (2001)
- Bagge-Hansen M et al. *J. Appl. Phys.* **117** 245902 (2015)
- Ten K A et al. *Nucl. Instrum. Meth. Phys. Res. A* **603** (1–2) 160 (2009)
- Pruel E R et al., in *Proc. 14th Intern. Detonation Symp., IDS 2010* p. 345
- Titov V M et al. *Combustion, Explosion and Shock Waves* **47** 615 (2011)
- Milyavskiy V V et al. *J. Appl. Sci.* **11** 1453 (2011)
- Merzhievsky L A et al. *Nucl. Instrum. Meth. Phys. Res. A* **603** 164 (2009)
- Shmakov A N, Vinokurov Z A *Zh. Strukt. Khim.* (6) (2016)
- Aulchenko V M et al. *Nucl. Instrum. Meth. Phys. Res. A* **603** 76 (2009)
- Ancharov A I et al. *Nucl. A* **470** 80 (2001)
- Sharafutdinov M et al. *J. Synchrotron Radiation* **10** 384 (2003)
- Sharafutdinov M R et al. *Nucl. Instrum. Meth. Phys. Res. A* **575** 149 (2007)
- Rogachev A S et al. *Nucl. Instrum. Meth. Phys. Res. A* **575** 126 (2007)
- Shkodich N F et al. *Bull. Russ. Acad. Sci. Phys.* **71** 650 (2007); *Izv. Ross. Akad. Nauk Fiz.* **71** 674 (2007)
- Yagubova I Yu et al. *Bull. Russ. Acad. Sci. Phys.* **71** 270 (2007); *Izv. Ross. Akad. Nauk Fiz.* **71** 278 (2007)
- Rogachev A S et al. *Crystallogr. Rep.* **48** 466 (2003); *Kristallogr.* **48** 511 (2003)
- Fedotov M G et al. *Nucl. Instrum. Meth. Phys. Res. A* **470** 245 (2001)
- Evdokov O V et al. *Nucl. Instrum. Meth. Phys. Res. A* **470** 236 (2001)
- Rubtsov I A et al., in *Zababakhinskie Nauchnye Chteniya, Sbornik Materialov XIII Mezhdunarodnoi Konf. (Zababakhin Scientific Readings. Proc. XIII Intern. Conf.)* (2017) p. 94
- Tolochko B P et al. *Diamond Related Mater.* **16** 2014 (2007)
- Ten K A et al. *Nucl. Instrum. Meth. Phys. Res. A* **603** 102 (2009)
- Ten K A et al. *Proc. 14th Intern. Detonation Symp., 2010*, p. 387
- Titov V M et al. *Diamond Related Mater.* **16** 2009 (2007)
- Tolochko B P et al. *Phys. Met. Metallog.* **105** (2) 134 (2008)
- Simentsova I I et al. *Kinet. Katal.* **53** (4) 520 (2012)
- Shmakov A N, Pod'yacheva O Yu *Zh. Strukt. Khim.* **55** 826 (2014)
- Pod'yacheva O Yu et al. *Catal. Today.* **147** 270 (2009)
- Ivanov M G et al. *J. Therm. Anal. Calorim.* **100** 79 (2010)
- Ivanov M G et al. *Solid State Phenomena* **163** 38 (2010)
- Ivanov M G et al. *Zh. Strukt. Khim.* **51** S52 (2010)
- Timchenko N A et al. *Izv. Vyssh. Uchebn. Zaved. Fiz.* **54** 190 (2011)
- Kosova N V et al. *Solid State Ionics* **225** 564 (2012)
- Tolochko B P, Maslii A I, Sheromov M A *Izv. Sib. Otd. Akad. Nauk SSSR Khim.* (1) 48 (1985)
- Lyakhov N Z, Maslii A I, Tolochko B P, Sheromov M A *Nucl. Instrum. Meth. Phys. Res. A* **261** 209 (1987)
- Tolochko B P, Maslii A I, Lyakhov N Z *Izv. Sib. Otd. Akad. Nauk SSSR Khim.* (1) 54 (1985)
- Sharafutdinov M R, Tolochko B P, Lyakhov N Z *Nucl. Instrum. Meth. Phys. Res. A* **470** 228 (2001)
- Avvakumov E G *Mekhanokhimicheskie Metody Aktivatsii Khimicheskikh Protessov* (Mechanochemical Methods for Activation of Chemical Processes) (Novosibirsk: Nauka, 1986)
- Evdokov O V, Titov V M, Tolochko B P, Sharafutdinov M R *Nucl. Instrum. Meth. Phys. Res. A* **603** 194 (2009)
- Bessergenev A V, Tolochko B P, Sheromov M A, Mezenchev N A *Nucl. Instrum. Meth. Phys. Res. A* **359** 160 (1995)
- Zhukovskii V M, Petrov A N *Zh. Prikl. Khim.* **46** (10) 2159 (1973)
- Tkachenko E V, Zhukovskii V M *Zh. Prikl. Khim.* **46** (10) 2129 (1973)
- Boldyrev V V *Difraktometriya s Ispol'zovaniem Sinkhrotronnogo Izlucheniya* (Diffraction with the Use of Synchrotron Radiation) (Ed. G N Kulipanov) (Novosibirsk: Nauka, 1989) p. 144
- Lars Kihlberg *Adv. Chem.* **39** (3) 37 (1963)
- Bokhonov B B et al. *J. Imaging Sci. Technol.* **51** 386 (2007)
- Bokhonov B B et al. *J. Phys. Chem. C* **118** 11980 (2014)
- Ancharov A I et al. *Poverkhnost. Rentgenovskie, Sinkhrotronnnye Neitronnye Issledovaniya* (7) 25 (2002)
- Ancharov A I, Grigorieva T F *Nucl. Instrum. Meth. Phys. Res. A* **543** 139 (2005)
- Ancharov A I et al. *Neorg. Mater.* **42** (10) 1164 (2006)
- Ancharov A I et al. *Russ. Metall.* **2006** 143 (2006); *Metally* (2) 55 (2006)